PGC1α is required for the renoprotective effect of lncRNA Tug1 *in vivo* and links Tug1 with urea cycle metabolites

Li Li[1,2,7], **Jianyin Long**[1,7], **Koki Mise**[1,3], **Daniel L. Galvan**[1], **Paul A. Overbeek**[4], **Lin Tan**[5], **Shwetha V. Kumar**[5], **Wai Kin Chan**[5], **Phillip L. Lorenzi**[5], **Benny H. Chang**[1], **Farhad R. Danesh**[1,6,8,*]

[1]Section of Nephrology, Division of Internal Medicine, The University of Texas MD Anderson Cancer Center, Houston, TX 77030, USA

[2]Department of Nephrology, The Second Xiangya Hospital, Central South University, Changsha, Hunan 410011, China

[3]Department of Nephrology, Rheumatology, Endocrinology and Metabolism, Okayama University Graduate School of Medicine, Dentistry and Pharmaceutical Sciences, Okayama, Japan

[4]Department of Molecular and Cellular Biology, Baylor College of Medicine, Houston, TX 77030, USA

[5]Metabolomics Core Facility, Department of Bioinformatics and Computational Biology, The University of Texas MD Anderson Cancer Center, Houston, TX 77030, USA

[6]Department of Pharmacology and Chemical Biology, Baylor College of Medicine, Houston, TX 77030, USA

[7]These authors contributed equally

[8]Lead contact

SUMMARY

lncRNA taurine-upregulated gene 1 (Tug1) is a promising therapeutic target in the progression of diabetic nephropathy (DN), but the molecular basis of its protection remains poorly understood. Here, we generate a triple-mutant diabetic mouse model coupled with metabolomic profiling data to interrogate whether Tug1 interaction with peroxisome proliferator-activated receptor gamma coactivator 1α (PGC1α) is required for mitochondrial remodeling and progression of DN *in vivo*. We find that, compared with diabetic conditional deletion of *Pgc1a* in podocytes alone (*db/db*;

Pgc1α$^{Pod-f/f}$), diabetic *Pgc1a* knockout combined with podocyte-specific Tug1 overexpression (*db/db*; Tug^{PodTg}; Pgc1α$^{Pod-f/f}$) reverses the protective phenotype of Tug1 overexpression, suggesting that PGC1α is required for the renoprotective effect of Tug1. Using unbiased metabolomic profiling, we find that altered urea cycle metabolites and mitochondrial arginase 2 play an important role in Tug1/PGC1α-induced mitochondrial remodeling. Our work identifies a functional role of the Tug1/PGC1α axis on mitochondrial metabolic homeostasis and urea cycle metabolites in experimental models of diabetes.

Graphical Abstract
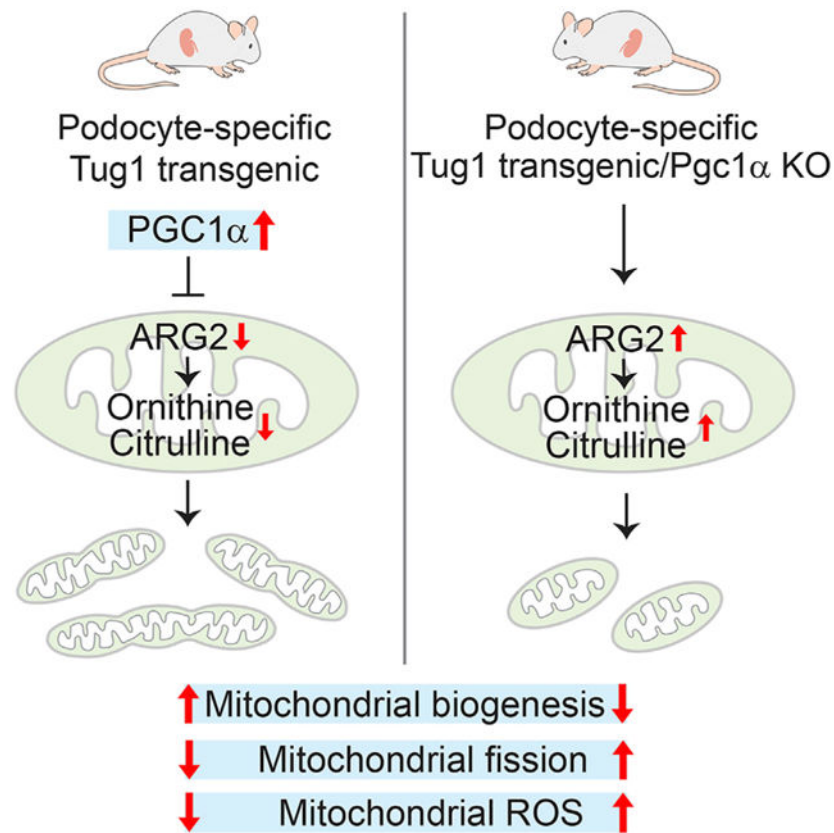
In brief

Li et al. show that PGC1α is required for the protective effects of lncRNA Tug1 on mitochondrial function in podocytes and progression of diabetic nephropathy *in vivo*. They find that altered urea cycle metabolites and mitochondrial arginase 2 (Arg2) play important roles in Tug1/PGC1α-induced mitochondrial remodeling.

INTRODUCTION

It is widely recognized that mitochondrial dysfunction contributes to the pathogenesis and progression of diabetic nephropathy (DN) (Forbes and Thorburn, 2018; Galvan et al., 2017; Hallan and Sharma, 2016), but the underlying molecular mechanisms that contribute to impaired mitochondrial function in DN *in vivo* remain incompletely understood.

Among several potential mechanisms implicated in mitochondrial dysfunction, we recently discovered that aberrant expression of lncRNA (long noncoding RNA) Tug1 (taurine-upregulated gene 1) plays a central role in promoting mitochondrial dysfunction in DN (Long et al., 2016).

lncRNAs are defined as various transcripts longer than 200 nucleotides that are classically not translated into proteins or encode very short peptides (Ransohoff et al., 2018; Ulitsky and Bartel, 2013). Along with advances in RNA biology, lncRNAs are known to play vital roles in regulating gene expression and participate in various physiological and pathological processes (Statello et al., 2021), including a growing appreciation of their role in kidney diseases such as DN (Kato and Natarajan, 2019; Kato et al., 2016; Li and Susztak, 2016; Long et al., 2016; Long and Danesh, 2018; Sun et al., 2018).

We had previously shown that Tug1 expression is reduced in the podocytes of several experimental models of diabetes, and podocyte-specific overexpression of lncRNA Tug1 in diabetic *db/db* mice mitigated progression of DN (Long et al., 2016). Associations were made between lncRNA Tug1 and low podocyte levels of Pgc1α (peroxisome proliferator-activated receptor gamma coactivator 1α) (Long et al., 2016), a well-characterized master regulator of mitochondrial biogenesis. But the underlying *in vivo* mechanisms remained elusive, and definitive evidence of a role for PGC1α as the downstream effector of Tug1 in animal models of DN was lacking.

Recent work indicates that PGC1α is highly expressed in the kidney and its expression is reduced in acute kidney injury (AKI) and several experimental models of chronic kidney diseases (CKDs) (Han et al., 2017; Tran et al., 2016). Although these studies have clearly shown the protective effect of PGC1α in different experimental models of AKI and CKDs, the direct role of PGC1α in the progression of DN *in vivo* is surprisingly poorly understood. Several studies have employed pharmacological activation of PGC1α to restore mitochondrial function and have reported protection against podocyte injury and progression of DN (Hong et al., 2018; Qi et al., 2017; Zhang et al., 2019; Zhou et al., 2019), whereas podocyte-specific Pgc1α transgenic mice were not protected from progression of DN in a streptozotocin model of DN (Li et al., 2017).

To address the *in vivo* role of PGC1α in Tug1-mediated renoprotection in DN, we generated genetically modified mouse models with transgenic expression of Tug1 combined with conditional deletion of Pgc1α in podocytes in diabetic *db/db* mice. Our findings suggest that PGC1α is required for the renoprotective effects of Tug1 and targeted ablation of Pgc1α in podocytes mitigates the protective effect of Tug1 on mitochondrial function and progression of DN *in vivo*. We also identified that altered urea cycle metabolites play an important role in Tug1/PGC1α-induced mitochondrial remodeling. These findings not only add to our current understanding of the impact of Tug1/PGC1α signaling *in vivo* but also provide a rationale for a promising treatment strategy to manipulate urea cycle intermediates by targeting lncRNA Tug1 in patients with DN.

RESULTS

Conditional Pgc1α deficiency in podocytes does not exacerbate progression of DN

Whether PGC1α is required for the renoprotective effects of lncRNA Tug1 in the diabetic milieu *in vivo* remains unknown. To determine whether the renoprotective features observed in the Tug1 transgenic mice were attributable to PGC1α *in vivo*, we examined the possibility of a genetic interaction between Tug1 and Pgc1α on mitochondrial remodeling and progression of DN. We conditionally deleted Pgc1α in podocytes, alone or in combination with podocyte-specific lncRNA Tug1 overexpression, in diabetic *db/db* mice. We generated inducible podocyte-specific Pgc1α-deficient mice (Pgc1α$^{f/f}$; podocin-iCreER^{T2}) by crossing floxed Pgc1α mice (Pgc1α$^{f/f}$) (Lin et al., 2004) with tamoxifen-inducible Cre transgenic mice, in which expression of Cre recombinase is driven by the human podocin promoter (podocin-iCreER^{T2}) (Ayanga et al., 2016; Wang et al., 2010) (Figures 1A and S1A). qRT-PCR, western blot analysis, and immunofluorescence analysis confirmed substantially reduced PGC1α (~10% residual RNA and protein) in podocytes isolated from Pgc1α$^{f/f}$; podocin-iCreER^{T2} mice (called Pgc1α$^{Pod-f/f}$) with tamoxifen induction relative to noninduced podocytes (Figures 1B, 1C, S1B, and S1C). However, PGC1α deletion did not lead to compensatory changes in PGC1β abundance based on western blot analysis (Figures S1B and S1C). We found that Pgc1α$^{Pod-f/f}$ mice were born at the expected Mendelian ratio and did not exhibit overt abnormalities. Furthermore, no significant differences were observed in urine albumin excretion (UAE) (20.85 ± 2.97 versus 16.63 ± 2.94 μg/24 h, p = 0.37), albumin-to-creatinine ratio (ACR) (65.57 ± 6.23 versus 55.23 ± 14.85 μg/mg, p = 0.94), and kidney histology after tamoxifen induction (Figures S1D–S1F). We did not detect mitochondrial morphology and dynamic changes by transmission electron microscopy (TEM) (Figures 1H–1J). Altogether, these results indicate that conditional deletion of Pgc1α in podocytes does not result in an obvious phenotype in physiological conditions. These findings are not surprising considering previously published literature related to the effect of Pgc1α knockdown in podocytes (Brinkkoetter et al., 2019) and the notion that many mutant mouse models need to be stressed *in vivo* to exhibit a phenotype.

We next sought to determine the effect of conditional Pgc1α deletion in podocytes on mitochondrial remodeling and progression of DN. To this end, we crossed Pgc1α$^{Pod-f/f}$ mice with Lepr$^{db/+}$ mice, an established model of type 2 diabetes, to generate Lepr$^{db/db}$; Pgc1α$^{Pod-f/f}$ mice (hereafter called db/db; Pgc1α$^{Pod-f/f}$) (Figure S2A). Tamoxifen-induced diabetic db/db; Pgc1α$^{Pod-f/f}$ mice displayed similar body weight and blood glucose in comparison to noninduced diabetic controls (Figures S2B and S2C). Furthermore, tamoxifen-induced diabetic Pgc1α$^{Pod-f/f}$ mice did not exhibit significant changes in the amount of albuminuria (453.70 ± 20.50 versus 409.80 ± 43.78 μg/mg, p = 0.54) or key histological findings, including mesangial matrix expansion and podocyte loss, compared with noninduced diabetic controls as measured by ACR, Wilms tumor protein 1 (WT1), and periodic acid-Schiff (PAS) staining (Figures 1D–1G). Consistently, TEM analysis showed similar podocyte foot process effacement and glomerular basement membrane (GBM) thickening in tamoxifen-induced and noninduced db/db; Pgc1α$^{Pod-f/f}$ mice (Figure 1E). Consistent with these findings, ultrastructure examination of mitochondria revealed similar

changes in mitochondrial morphology, with similar aspect ratio (AR) and form factor (FF) values in tamoxifen-induced versus noninduced diabetic Pgc1α$^{Pod-f/f}$ mice (Figures 1H–1J). Altogether, these data demonstrated that podocyte-specific deletion of Pgc1α did not exacerbate progression of DN or mitochondrial dysfunction in the diabetic environment. Our interpretation of these findings is that because PGC1α is already downregulated in DN, further downregulation of its expression does not alter the course of DN or mitochondrial morphology in diabetic kidneys.

PGC1α is required for the renoprotective effect of Tug1 *in vivo*

We had previously shown that Tug1 expression was reduced in the podocytes of several experimental models of diabetes and podocyte-specific overexpression of Tug1 in diabetic mice improved the biochemical and histological features associated with DN (Long et al., 2016). We also provided evidence from *in vitro* cell-based assays that PGC1α could serve as a target of Tug1 in the diabetic milieu (Long et al., 2016). We next asked whether PGC1α is required for the renoprotective effects of podocyte-specific overexpression of lncRNA Tug1 in the diabetic milieu *in vivo*. To address our main hypothesis, we crossed Pgc1α$^{Pod-f/f}$ mice with our previously generated Tug^{PodTg} mice (Long et al., 2016) to generate a conditional inducible diabetic db/db; Tug^{PodTg}; Pgc1α$^{Pod-f/f}$ mutant mouse (Figure 2A). We allocated our triple-mutant diabetic mice to three groups: control db/db; Pgc1α$^{Pod-f/f}$, noninduced diabetic db/db; Tug^{PodTg}; Pgc1α$^{Pod-f/f}$, and tamoxifen-induced diabetic db/db; Tug^{PodTg}; Pgc1α$^{Pod-f/f}$. As expected, qPCR analysis of podocytes from diabetic Tug^{PodTg} mice showed a significant increase in Tug1 expression in podocytes independent of PGC1α (Figure 2B). We observed a five-fold increase in Pgc1α mRNA expression in podocytes from noninduced diabetic Tug^{PodTg}; Pgc1α$^{Pod-f/f}$, whereas tamoxifen-induced diabetic Tug^{PodTg}; Pgc1α$^{Pod-f/f}$ exhibited significant knockdown of Pgc1α expression (~90%) (Figure 2B). As an additional control, we also assessed multiple known downstream target genes of PGC1α, including *Tfam*, *Nrf1*, *Nrf2* (or *Gapba*), and *Esrra*, and found that they were similarly downregulated in podocytes from tamoxifen-induced diabetic Pgc1α$^{Pod-f/f}$ mice relative to podocytes from noninduced diabetic Tug^{PodTg} (Figure S3A).

We observed no statistically significant changes in body weight and blood glucose among the three groups (Figures 2C and 2D); however, Tug1 overexpression in podocytes led to reduced albuminuria and mesangial matrix expansion in the glomeruli (Figures 2E–2H). These beneficial effects of Tug1 overexpression were partially reversed in tamoxifen-induced triple transgenic diabetic Tug^{PodTg}; Pgc1α$^{Pod-f/f}$ mice. TEM revealed that Pgc1α knockout mitigated the observed improvement of Tug1 overexpression on podocyte foot process effacement and GBM thickening (Figures 2G and 2J). In addition, increased podocyte number in mice with Tug1 overexpression was reduced by approximately 85% in glomeruli from tamoxifen-induced diabetic db/db; Tug^{PodTg}; Pgc1α$^{Pod-f/f}$ mice (Figures 2G and 2I).

We next tested whether the effects of Tug1 on mitochondrial homeostasis are also mediated by PGC1α *in vivo*. We focused on four key features of mitochondrial function: mitochondrial biogenesis, dynamics, redox, and bioenergetics. Importantly, mitochondrial ultrastructure examination by electron microscopy revealed more fragmented mitochondria

with decreased AR and FF in podocytes from tamoxifen-induced diabetic Tug^{PodTg}; Pgc1α$^{Pod-f/f}$ mice in comparison to mitochondria in noninduced diabetic mice (Figures 3A–3D). Because of significant changes in mitochondrial morphology, we next assessed the role of the Tug1/PGC1α axis on fusion and fission regulatory proteins. We found that the transcription levels of key mitochondrial fission proteins, including *Drp1* (dynamin-related protein-1), *Fis1* (mitochondrial fission protein 1), *Mff* (mitochondrial fission factor), and *MiD49* and *MiD51* (mitochondrial dynamic proteins of 49 and 51 kDa) were significantly decreased, whereas *Mfn1* (mitofusin 1) and *Mfn2* (mitofusin 2), key components of mitochondrial fusion, were upregulated in podocytes from Tug1 transgenic mice (Figure 3E), indicating enhanced mitochondrial fusion and decreased fragmentation with Tug1 overexpression. However, the protective properties of Tug1 were mitigated when Pgc1α was knocked down in podocytes in induced db/db; Tug^{PodTg}; Pgc1α$^{Pod-f/f}$ mice, suggesting that PGC1α is necessary for the modulatory effects of Tug1 on mitochondrial morphology.

Consistent with these observations, we observed a reversal of the effect of Tug1 overexpression relative to podocytes obtained from Tug1 overexpression combined with Pgc1α knockdown in diabetic mice on mitochondrial biogenesis, as assessed by mitochondrial copy number (177.42% ± 8.44% versus 82.29% ± 4.15%, p < 0.001), mitochondrial ROS (reactive oxygen species) as measured by MitoSOX (2,042.46 ± 244.02 versus 5,455.57 ± 334.43, p < 0.001), and total ATP production (149.62% ± 2.24% versus 105.15% ± 3.60%, p < 0.001) (Figures 3F–3H and S3B).

We then tested the effects of the Tug1/PGC1α axis on mitochondrial bioenergetics by directly measuring the oxygen consumption rate (OCR) and extracellular acidification rate (ECAR). We found that basal respiration and maximal OCR were 1.28-fold and 1.4-fold higher, respectively, in podocytes with Tug1 overexpression compared with control noninduced db/db; Pgc1α$^{Pod-f/f}$ podocytes. Silencing of Pgc1α in podocytes of diabetic mice with Tug1 overexpression prevented the effects of Tug1 on both basal and maximal respiration rates (Figures 3I–3K). We also found basal glycolysis, glycolytic capacity, and glycolytic reserve were 1.68-fold, 2.17-fold, and 2.2-fold lower, respectively, as assessed by ECAR, in podocytes with Tug1 overexpression compared with control noninduced db/db; Pgc1α$^{Pod-f/f}$ podocytes. Although no statistically significant differences were found in basal acidification rates and glycolytic reserve, decreased glycolytic capacity was reversed in podocytes in diabetic mice with Pgc1α knockout and Tug1 overexpression (Figures 3L–3O). Altogether, our findings suggest that PGC1α is required for the protective effect of Tug1 on mitochondria and progression of DN. Indeed, our data provided clear evidence that the Tug1/PGC1α axis plays a central role on reprogramming of mitochondrial biogenesis, bioenergetics, redox, and morphology induced by the diabetic environment.

Urea cycle intermediates link the Tug1/PGC1α axis with mitochondrial remodeling

In response to external metabolic cues, cells are known to exhibit metabolic remodeling, characterized by their ability to adapt to changes in metabolic demand by shifting between substrates and/or metabolic pathways. To further understand the role of Tug1 on key metabolic pathways, we initially reanalyzed our previously deposited unbiased comparative transcriptome analyses between stable Tug1-knockdown (shTug1) and scramble short

hairpin RNA (shRNA) control (shCtrl) podocytes (Long et al., 2016), which provided some early clues to a range of mRNA alterations of enzymes catalyzing reactions in glycolysis, the TCA (tricarboxylic acid) cycle, and oxidative phosphorylation (OXPHOS) (Figure 4A). We identified significant mRNA expression changes in several glycolytic enzymes (*Aldh2*, *Pck2*, *Pfkl*, *Pgam1*, *Pgk1*, and *Bpgm*) that were more than 2-fold increased, whereas several OXPHOS-related genes were significantly decreased, including TCA enzyme *Ogdh* and subunits of mitochondrial respiratory chain complex I, II, III, and IV. These findings are suggestive of enhanced glycolysis and decreased OXPHOS activity in shTug1 cells (Figure 4A).

We next challenged our observations by directly measuring the effect of Tug1/PGC1α on mitochondrial metabolite profiles in podocytes. Mitochondrial metabolites play key roles in a myriad of metabolic pathways, including glycolysis, the pentose phosphate pathway, the TCA cycle, and nonessential amino acid synthesis (Martínez-Reyes and Chandel, 2020). The role of Tug1 on mitochondrial metabolites is unknown, and although the effects of PGC1α as a master regulator of mitochondrial biogenesis and bioenergetics are well established, its role on mitochondrial metabolites is less understood.

We initially leveraged our previously established stable Tug1-knockdown (Tug1-KD) podocyte cell line (Long et al., 2016) to further assess the role of Tug1/PGC1α on mitochondrial metabolites in podocytes. We also generated a double mutant of Pgc1α overexpression with Tug1-KD (Tug1-KD/Pgc1-OE) cell line to assess whether Pgc1α overexpression in podocytes can rescue the effect of Tug1-KD on metabolic pathways (Figure S4). We first validated whether cultured podocytes phenocopy our *in vivo* findings on mitochondrial bioenergetics by assessing their impact on both ECAR and OCR analyses. We found that double-mutant Tug1-KD/Pgc1-OE rescued the effects of Tug1-KD on basal, maximal, and spare-capacity respiration rates in podocytes (Figures S5A–S5D), suggesting that our mutant cell lines can be further used to gain mechanistic insights.

We next employed unbiased metabolomic analysis based on liquid chromatography-mass spectrometry (LC-MS) for both whole-cell and mitochondria metabolites to gain insight into the role of the Tug1/PGC1α axis on metabolite profiles in podocytes. Among measured intermediates of glycolysis, the TCA cycle, and amino acids, we found that intermediates of the urea cycle (also known as the arginine-citrulline cycle) are the most prominently altered by both Tug-KD and Tug1-KD/Pgc1-OE cell lines (Figure 4B). We found that ornithine and citrulline, two intermediates of this urea cycle, were the most upregulated metabolites in Tug1-KD cells relative to control cells, whereas the same metabolites were among the most reduced metabolites in Tug1-KD/Pgc1-OE podocytes relative to Tug1-KD cells, suggesting a modulatory effect of the Tug1/PGC1α axis on these two key metabolites (Figures 4C and 4D). Metabolite set enrichment analysis also indicated pyrimidine metabolism, a downstream byproduct of the urea cycle and arginine biosynthesis among the most overrepresented pathways (Figures 4E and 4F).

To explore how the Tug1/PGC1α axis regulates the metabolism of ornithine and citrulline, we assessed several key enzymes in the urea cycle, including argininosuccinate synthetase (ASS1), argininosuccinate lyase (ASL), arginase 1 and arginase 2 (ARG1 and ARG2), and

nitric oxide synthases (NOS1, NOS2, and NOS3). We detected very low expression of Cps1 (carbamoyl phosphate synthetase 1), Otc (ornithine transcarbamylase), Nos1, and Nos3 in podocytes (Table S1); hence, we concentrated on other key enzymes of the cycle. qRT-PCR and western blot analyses of the remaining enzymes indicated high ARG2 expression coupled with low ASS1, ASL, ARG1, and NOS2 in Tug1-KD cells, whereas Pgc1-OE reversed the effect of Tug1-KD on the expression of all these enzymes (Figures 5A and 5B). We focused on the mitochondrial ARG2 enzyme and argued that enhanced ARG2 expression/activity could link some mitochondrial effects of the Tug1/PGC1α axis with increased ornithine and mitochondrial metabolites.

In mammals, two isoforms of arginase exist: ARG1 is a cytosolic enzyme, whereas ARG2 is targeted to the mitochondria and is the predominant isoform expressed in kidney cells (Morris et al., 2011; Vockley et al., 1996). ARG2 is required for the conversion of L-arginine into ornithine, and importantly, elevated ARG2 expression has been previously reported in DN (Morris et al., 2011; You et al., 2013).

To test whether ARG2 expression/activity links some mitochondrial effects of the Tug1/PGC1α axis, we first measured arginase activity in our podocyte samples. Compared with control, Tug1-KD exhibited increased arginase activity, whereas arginase activity returned to baseline levels in Tug1-KD/Pgc1-OE podocytes (Figure 5C). In complementary experiments, we validated arginase activity in primary podocytes isolated from tamoxifen-induced and noninduced db/db; Tug^{PodTg}; Pgc1α$^{Pod-f/f}$ mice. We found that Tug1 overexpression led to decreased arginase activity, whereas podocyte-specific Pgc1α knockout abolished this protective effect (Figure 5D). Next, to further understand the relevance of ARG2, we evaluated whether ARG2 could mediate the effect of the Tug1/PGC1α axis on mitochondrial remodeling in DN. To this end, we used an Arg2 small interfering RNA (siRNA) (siArg2) and showed that podocytes treated with siArg2 exhibited a significant lower level of ARG2 expression (Figure S5E). We found that primary tamoxifen-induced db/db; Tug^{PodTg}; Pgc1α$^{Pod-f/f}$ podocytes transfected with Arg2 siRNA exhibited similar ATP and bioenergetics relative to tamoxifen-induced db/db; Tug^{PodTg}; Pgc1α$^{Pod-f/f}$ podocytes transfected with a nontargeting siRNA control (Figures 5E and 5F). However, mitochondrial biogenesis (Figure 5G), ROS production (Figure 5H), and dynamics (Figures 5I and 5J) were significantly changed in tamoxifen-induced db/db; Tug^{PodTg}; Pgc1α$^{Pod-f/f}$ podocytes transfected with Arg2 siRNA, relative to tamoxifen-induced db/db; Tug^{PodTg}; Pgc1α$^{Pod-f/f}$ podocytes transfected with a nontargeting siRNA control, and partially reversed to the mitochondrial phenotype observed in noninduced db/db; Tug^{PodTg}; Pgc1α$^{Pod-f/f}$ podocytes. This suggests that ARG2 partly mediates the effects of Tug1/PGC1α on mitochondrial biogenesis, ROS production, and dynamics, but not on mitochondrial bioenergetics and ATP production. We found similar results with cultured podocytes transfected with siArg2 (Figures S5F–S5I). We also challenged Tug1-KD/Pgc1-OE podocytes with different concentrations of ornithine (5 and 10 mM), citrulline (3 and 10 mM), or arginine (3 and 10 mM). Exogenous ornithine and citrulline supplementation in higher concentrations reversed Tug1-KD/Pgc1-OE-induced enhanced mitochondrial biogenesis, whereas addition of arginine had no significant effect on mitochondrial copy number (Figure S5J).

Finally, because PGC1α is a transcriptional coactivator that transcriptionally modulates expression of multiple genes involved in mitochondrial homeostasis, we explored whether the Tug1/PGC1α axis is involved in Arg2 transcription. To this end, we subcloned the 1-kb proximal promoter of the mouse *Arg2* gene into a luciferase reporter construct and assessed the promoter activity with transient expression of either Tug1 or Pgc1α. We found that Arg2 promoter-driven luciferase activities were significantly repressed by both Tug1 and Pgc1α in a dose-dependent manner (Figure 5K), suggesting that both Tug1 and PGC1α could negatively regulate the transcription of Arg2.

Altogether, these results indicate that the Tug1/PGC1α axis relies on urea cycle metabolites and ARG2 activity to affect several key features of mitochondrial metabolic fitness of podocytes in the diabetic milieu. Our results suggest that the Tug1/PGC1α axis negatively regulates arginase 2 expression at both mRNA and protein levels and could modulate the enzymatic activity of ARG2.

DISCUSSION

In this study, we report a central role of lncRNA Tug1 in regulating PGC1α and mitochondrial metabolism in DN *in vivo*. Our data also indicate that podocyte-specific Pgc1α deficiency reverses the Tug1-induced renoprotective phenotype in a model of type 2 diabetes. Our findings highlight the multifaceted contributions of the lncRNA Tug1/PGC1α axis on the composition and function of mitochondria in podocytes in the diabetic milieu. Our results suggest that PGC1α-dependent renoprotective effects of Tug1 on mitochondrial fitness come through at least six distinct mechanisms: improving mitochondrial biogenesis, correcting mitochondrial dynamics, enhancing mitochondrial bioenergetics, mitigating mitochondrial ROS, and remodeling of the mitochondrial metabolites and biosynthetic properties of mitochondria.

PGC1α has been well established as playing central roles in mitochondrial energy production, biogenesis, and bioenergetics. PGC1α has also been implicated in regulating mitochondrial morphology and dynamics (Martin et al., 2014; Singh et al., 2016). Our findings suggest that the Tug1/PGC1α axis has an important role in regulating mitochondrial dynamics by reducing diabetes-associated enhanced mitochondrial fission through downregulation of Drp1, Fis1, and Mff and increasing Mfn1 and Mfn2 expression in podocytes (Ayanga et al., 2016; Galvan et al., 2019).

Using metabolomic and functional approaches, we discovered that the Tug1/PGC1α axis appears to be differentially regulating the urea metabolites, leading to a significant increase in ornithine and citrulline concentration. The urea cycle is composed of several enzymes, including ASS1, ASL, ARG1, ARG2, and OTC, which supply the cells with the synthesis of polyamines, nitric oxide, proline, and pyrimidine, all essential for cell survival and proliferation (Caldwell et al., 2018). In addition, the urea cycle is intimately linked with other central metabolic processes, such as the TCA cycle (Fu et al., 2020; Xu et al., 2016). Although an association between urea cycle metabolites and DN has been previously reported (Darshi et al., 2016; Hirayama et al., 2012), the extent to which urea cycle metabolites contribute to Tug1/PGC1α-induced mitochondrial remodeling in DN

and its effect on podocyte function in DN has not been previously explored. Given that mitochondrial metabolites play critical roles in many pathologies, ornithine and/or citrulline of the urea cycle metabolites may serve as promising therapeutic targets in DN. It will be important for future studies to probe the mitochondrial metabolite concentrations in patients with DN to better understand the urea cycle intermediates and mitochondrial enzymes that could be potentially critical to DN progression.

Two isoforms of arginase, ARG1 and ARG2, which are encoded by different genes and differ in their tissue distribution and intracellular location, are key allosteric regulators of the urea cycle (Grody et al., 1989; Vockley et al., 1996). ARG1 is a cytosolic enzyme, whereas ARG2 is targeted to the mitochondria and is expressed in many tissues, including the kidney (Morris et al., 1997). ARG2 has an important role in the synthesis of ornithine, and there is some evidence that ARG2 can play a central role in the progression of microvascular complications of diabetes (Morris et al., 2011; Wetzel et al., 2020; You et al., 2013). Importantly, we found that Arg2 plays a critical role in Tug1/PGC1α-mediated regulation of mitochondrial biogenesis, mitochondrial ROS production, and mitochondrial dynamics, but not mitochondrial bioenergetics and ATP. We speculate that the effects of ARG2 on these key mitochondrial functions result from its modulatory effect on ornithine production in the mitochondria. However, the underlying molecular effects of ornithine on mitochondrial remodeling remain largely unknown, and intensive studies in our lab are under way to unravel the molecular mechanism by which ornithine could affect mitochondrial function and DN progression. We also recognize that there are limitations to mechanistic studies using animal models of DN. However, we were careful in this study and previous studies to examine multiple model systems to further understand the impact of Tug1/PGC1α on DN progression (Long et al., 2016).

Altogether, our findings identify an important but previously unappreciated functional role of the lncRNA Tug1/PGC1α axis on mitochondrial homeostasis and urea cycle metabolites in experimental models of diabetes. Understanding how Tug1 regulates mitochondrial metabolites and progression of DN provides several potential targets to modulate cell metabolites and the severity of DN.

STAR★METHODS

RESOURCE AVAILABILITY

Lead contact—Further information and requests for resources and reagents should be directed to and will be fulfilled by the lead contact, Dr. Farhad Danesh (fdanesh@mdanderson.org).

Materials availability—Plasmids generated in this study will be available upon request with material transfer agreements.

Data and code availability

- Original metabolomics data generated for this study have been deposited to NIH Metabolomics Workbench Data Repository with the project identifier NMDR: PR001167.

- This paper does not report original code.

- Any additional information required to reanalyze the data reported in this paper is available from the lead contact upon request.

EXPERIMENTAL MODEL AND SUBJECT DETAILS

Animals—All animal studies were conducted according to the "Principles of Laboratory Animal Care" (NIH publication No. 85023, revised 1985) and the guidelines of the IACUC of The University of Texas MD Anderson Cancer Center. We obtained the diabetic db/db mice and their control littermates db/m (Strain # 000642, BKS.Cg-Dock7$^{m+/+}$Lepr$^{db/J}$) and Pgc1α floxed mice (Strain #009666, B6N.129 (FVB)-Ppargc1a$^{tm2.1Brsp}$/J) from Jackson Laboratories (Bar Harbor, ME); podocytes-specific Tug1 transgenic mice (Tug^{Podtg}) were described before (Long et al., 2016). Pgc1α-floxed mice were backcrossed 10 generations on C57BLKS background before bred with db/m mice. Podocin-iCreER^{T2} transgenic mice were generated in our laboratory previously (Wang et al., 2010) and were used to generate inducible podocyte-specific deletion of *Pgc1a*. These mice express ligand-dependent chimeric Cre recombinases (iCreER^{T2}) in the podocytes that can be activated by the synthetic estrogen receptor ligand 4-hydroxytamoxifen. For studies involving deletion of *Pgc1a* in podocytes, 8-week-old mice with appropriate genotype were administrated 4mg/d tamoxifen (Sigma-Aldrich, #T5648, dissolved in sesame oil) intraperitoneally for 10 days. Fasting blood glucose, body weight, and urine albumin levels were monitored at 8, 12, 16, and 20 weeks of age. Mice used for the experiments were 16 or 20 weeks old, unless otherwise specified. We used only male mice in experiments. All animals were maintained on a normal chow diet and housed in a room with a 12:12-hour light/dark cycle and an ambient temperature of 22°C.

Cell lines—We used conditionally immortalized mouse podocytes (MPC5) in this study as previously reported (Mundel et al., 1997). Briefly, podocytes were cultured on BD BioCoat Collagen I plates (BD Biosciences, San Jose, CA) at 33°C in RPMI 1640 complete media with 20 U/ml mouse recombinant IFN-γ (Thermo Fisher, Carlsbad, CA). To induce differentiation, we cultured podocytes in DMEM (5.5mM glucose and 5% FBS) at 37°C without IFN-γ for 10–12 days. To rescue the expression of PGC1α in stable Tug1-knockdown CRISPR clone (Tug1-KD)(Long et al., 2016), CMV enhancer/promoter-driven mouse *Pgc1a* cDNA (Addgene, Watertown, MA) was inserted into vector Zeo-pT-MCS-GFP-T2A-Puro(Long et al., 2020), a modified *PiggyBac* transposon system, selected with 1 μg/ml puromycin and sorted by GFP, to generate Tug1-KD/Pgc1-OE. We isolated kidney podocytes by positive selection with biotin-labeled Kirrel3 and Podocalyxin antibodies (2.5 μg/antibody/mouse, R&D Systems, Minneapolis, MN) followed by Streptavidin M-280 Dynabeads as previously described (Badal et al., 2016). We routinely measure podocytes marker Nephrin enrichment in the podocytes fraction to ensure the successful enrichment of podocytes isolation. Human embryonic kidney fibroblast 293T cells (CRL-3216) were obtained from ATCC and cultured according to the instructions at 37°C. All cell culture experiments were repeated independently at least three times.

METHOD DETAILS

Biochemical, histological and morphometric studies—We measured the urinary albumin using Albuwell M (Excocell, Philadelphia, PA, USA) according to manufacturer's instructions. For histological staining procedures, 5 μm thick formalin-fixed, paraffin-embedded kidney sections were deparaffinized and dehydrated using Histo-Clear and a series of increasingly concentrated ethanol washes. We performed PAS staining according to the manufacturer's guidelines (Sigma Aldrich, St Louis, MO, USA). For histological analysis, the investigators analyzing data were blinded to the group allocations. PAS and TEM data were examined by an independent pathologist, blinded to the experimental conditions. Quantification of Mesangial Matrix Expansion were determined using Adobe Photoshop CC 2020 software (Adobe Systems, Inc., San Jose, CA). At least three mice were analyzed per group, and 50 glomeruli were measured per mouse. Quantification of GBM Thickening were performed using ImageJ Software (version 1.53 g; National Institutes of Health, Bethesda, MD).

Seahorse metabolic analyzer assays—Primary or cultured podocytes were grown on 0.1 μg/ml Collagen I-coated plates in DMEM media supplemented with 5% FBS, 1% Antibiotic-Antimycotic. Cells were seeded onto a 96 well XFe96 microplate (part of Seahorse XFe96 FluxPak, Agilent) at a cell density of 3×10^4 cells/well, 2 days before assay to allow cells attachment. One day before the assay, cartridge plate (part of Seahorse XFe96 FluxPak, Agilent) was hydrated overnight with H_2O and replaced with Calibrant (Agilent) for at least 1hr in a non-CO_2 incubator. Cell plates were washed once with PBS and replaced with Seahorse Assay Medium (pH 7.4) (Agilent) and replaced again right before assay. Assay conditions and set up were performed using Mito Stress Test Kit and Glycolysis Stress Test Kit (Agilent) on a Seahorse XFe96 Analyzer (Agilent), according to manufacturer's instructions. All Seahorse assay data was analyzed using Seahorse Wave v2.6.1 Software (Agilent).

Mitochondrial morphology assessment—Mitochondrial fission and aspect ratio were measured by ImageJ as previously described (Galvan et al., 2019). The morphology of mitochondria was quantified by determining the area and the best-fitting ellipse yields the longitudinal length (major), equatorial length (minor). Subsequently, these parameters were used for the calculation of the aspect ratio to evaluate the elongation of mitochondria (Aspect ratio = major axis/minor axis). The form factor was defined as $(Pm^2)/(4\pi Am)$, where Pm is the perimeter and Am is the area of the mitochondrion. The morphology of at least 110 mitochondria was determined for each group.

For primary podocytes, cells were plated at 2×10^3 density on BioCoat Collagen I 22 mm coverslips and allow cells to attach before staining. Cells were incubated with 100nM MitoTracker Red CMXRos (Life technologies) for 20 minutes. After washed 3 times with DPBS, cells were fixed with ice-cold 1:1 methanol/acetone (v/v) and mounted. Images were acquired on a FV1200 confocal microscope (Olympus). The shape descriptor of more than 3000 mitochondrial particles was measured per experimental condition.

Mitochondrial DNA copy number, ROS and ATP determination—Genomic DNA was extracted from isolated primary podocytes or cultured podocytes using PureLink Genomic DNA Mini Kit (Thermo Fisher) according manufacturer's instructions. Mitochondrial DNA copy number was assayed as previously described (Long et al., 2016), using mouse mitochondrial ND1, mouse mitochondrial Cyt B, and mouse nuclear H19 DNA (Table S2). To test the effect of metabolites on mitochondrial copy number, podocytes were cultured in medium supplemented with assorted metabolites (ornithine, citrulline or arginine) for 48 hours at the indicated concentrations (Geiger et al., 2016; Ochocki et al., 2018). To measure mitochondrial ROS, we incubated podocytes at 37°C with fresh media without serum containing 5 μM MitoSOX Red mitochondrial superoxide indicator (Thermo Fisher). The cells were observed on confocal microscope and analyzed by flow cytometry with help from UT-MDACC FCCICF Core, as previously described (Wang et al., 2012). Cellular ATP levels were measured using the CellTiter-Glo Luminescent Cell Viability Assay Kit (Promega), as previously described (Long et al., 2016).

Arginase activity and arginase 2 promoter activity—We measured arginase activity by quantification of the rate of production of urea in the arginase reaction and expressed as nanomoles of urea produced per hour normalized to total protein, using a quantitative colorimetric kit (BioAssay Systems, Cat# DARG-100) according to manufactures' instructions with 2hrs incubation.

For arginase 2 promoter activity assay, we amplified and cloned a 1kb proximal promoter of murine arginase 2 gene (*Arg2*) from genomic DNA of C57BL/6J mouse (Jackson Laboratory) by PCR, using Phusion High Fidelity DNA Polymerase (New England Bio-labs) (Table S2). The 1038-bp PCR product was cloned between KpnI and XhoI site of promoter-less luciferase reporter vector pGL4.10 [luc2] (Promega, Madison, WI). Luciferase assays were carried out as described previously (Long et al., 2020). Briefly, 5×10^5 HEK293T cells on 12-well plates were transfected with firefly luciferase reporter, pGL4-luc vector or pGL4-Arg2-luc promoter construct, and renilla luciferase internal control pRL-TK (Promega), together with Tug1 or Pgc1α in pRK5 vector(Lin et al., 2006) for transient overexpression, using Lipofectamine 2000 (Thermo Fisher). Luminescence was measured using a Dual-Luciferase Assay System (BPS Bioscience) on a FLUOstar Omega luminometer.

Immunofluorescence—Formalin-fixed, paraffin-embedded tissue sections were cut at 5-μm thickness and mounted on slides. After deparaffinization and rehydration, these kidney sections were subjected to heat-induced epitope retrieval in Tris-EDTA Buffer (10mM Tris Base, 1mM EDTA Solution, pH 9.0) for 1h. Sections were washed twice with TBS and blocked in 1% BSA and 0.03% Triton X-100 in TBS for 1h at room temperature. After blocking, the sections were incubated overnight at 4°C with primary antibodies against PGC1α (Milli-pore, ST1202, 1/100), Synaptopodin (Progen, GP94-N,1/250), or WT1 (Abcam, ab89901, 1/50) in blocking buffer followed by 4×5 min washes in TBS. Tissue sections were then incubated with the following secondary antibodies: donkey anti-rabbit Alexa Fluor 488 (Thermo Fisher, A21206; 1/1000), donkey anti-mouse Alexa Fluor 594 (Thermo Fisher, A21203; 1/1000) or donkey anti-guinea pig Alexa Fluor 594 (Thermo

Fisher, A11076; 1/1000) for 1 hour at RT in blocking buffer. The sections were washed 3 times with TBS, and nuclei were counterstained with DAPI (Thermo Fisher, 62248). Finished slides were mounted with ProLong Gold Antifade Mounting Reagent (Thermo Fisher). Images were acquired on a FV1200 confocal microscope (Olympus). All images were acquired with the same settings for each channel. Podocytes were identified according to positivity of both WT1 and DAPI staining. Total numbers of podocytes were counted in 20 randomly selected kidney glomeruli per randomly selected animal. The data were presented as podocyte numbers relative to the corresponding glomerular area as assessed using ImageJ Software.

Western blot analysis—Podocytes pellets were lysed in RIPA Buffer (TEKnova, Hollister, CA) (50mM Tris-HCl, 150mM NaCl, 1% Triton X-100, 1% sodium deoxycholate, 0.1% SDS, 2mM EDTA, pH7.5) supplemented with protease inhibitor cocktails (Roche), and determined the protein concentration by DC Protein Assay (Bio-Rad, Hercules, CA). Twenty μg of total protein lysate was diluted in 5x Laemmli buffer, loaded on 4%–20% gradient SDS-PAGE (Bio-Rad) and transferred to nitrocellulose membranes. Membranes were probed with primary antibodies and corresponding secondary antibodies, followed by acquisition on Odyssey Fc Imaging System (Li-COR Biosciences, Lincoln, NE). We performed quantitative image analysis using Image Studio v4.0 Software (Li-COR Biosciences).

RNA extraction and RT-qPCR—Total RNAs were extracted using PureLink RNA Mini Kit (Thermo Fisher Scientific) with on-column digestion of DNase I (New England Biolabs, Ipswich, MA). After reverse transcription by random priming using iScript cDNA Synthesis Kit (Bio-Rad, Hercules, CA), cDNAs were diluted into 10ng per well and quantified by real-time PCR using PowerUp SYBR Green Master Mix (Thermo Fisher) on StepOnePlus Real-Time PCR System (Applied Biosystems). Individual samples were run in duplicate, and each experiment was repeated at least 3 times. We calculated the relative gene expression using the $2^{-\Delta\Delta CT}$ method (Livak and Schmittgen, 2001). The expression levels of all genes were normalized to *Gapdh* or *β-actin*. qPCR primers used in this study are listed in Table S2.

Transmission electron microscopy—Fixed samples were washed in 0.1 M cacodylate buffer, post fixed them with 1% buffered osmium tetroxide for 1 h, and stained them en bloc with aqueous 1% Millipore-filtered uranyl acetate. The samples were washed several times in water, then dehydrated in increasing concentrations of ethanol, infiltrated, and embedded in LX-112 medium. The samples were polymerized in a 60°C oven for about 3 days. Ultrathin sections were cut in a Leica Ultracut microtome (Leica, Deerfield, IL), stained with uranyl acetate and lead citrate in a Leica EM Stainer, and examined in a JEM 1010 transmission electron microscope (JEOL, USA, Inc., Peabody, MA) at an accelerating voltage of 80 kV. We obtained digital images-using AMT Imaging System (Advanced Microscopy Techniques Corp, Danvers, MA).

Analysis of polar metabolites by LC- and IC-HRMS—The relative abundance of polar metabolites in cell samples were analyzed by ultra–high resolution mass spectrometry (HRMS). Metabolites from cell samples (in triplicates) grown on 10cm dishes were

extracted with ice-cold 80% methanol. After centrifugation, extracts in supernatants were dried by evaporation under nitrogen, and reconstituted in deionized water, of which 5 μL was injected for analysis by ion chromatography (IC)-MS on Dionex ICS-5000+ System (Thermo Scientific). IC mobile phase A was water, mobile phase B was 100 mM KOH, mobile phase flow rate was 350 μl/min. For hydrophilic interaction chromatography (HILIC) analysis, we diluted samples in 90% acetonitrile (v/v) containing 1% formic acid, of which 15 μL was injected for analysis by liquid chromatography (LC)-MS on Vanquish LC System (Thermo Scientific). LC mobile phase A was acetonitrile containing 0.1% formic acid, and mobile phase B was 50 mM ammonium formate, mobile phase flow rate was 300 μl/min. All MS Data were acquired using Orbitrap Fusion Tribrid Mass Spectrometer (Thermo Scientific) under ESI positive ionization mode at a resolution of 240,000. We imported the raw data files to Trace Finder Software (Thermo Scientific) for final analysis. The relative abundance of each metabolite was normalized by sample DNA concentration.

QUANTIFICATION AND STATISTICAL ANALYSIS

Group data are expressed as mean ± SEM. We used one way-analysis of variance (one-way ANOVA) to perform comparisons of multiple groups followed by Tukey's multiple comparisons test. We performed *Student's t test* for comparisons between two groups. All tests were two-tailed, with a $p < 0.05$ considered to be a statistically significant result. Throughout the figures, asterisks denote statistical significance reported by the indicated statistic test (*$p < 0.05$; **$p < 0.01$; ***$p < 0.001$; ****$p < 0.0001$). We used GraphPad PRISM v8.0 to perform statistical analysis (GraphPad, San Diego, CA). Statistical details are shown in each of the figure legends.

Supplementary Material

Refer to Web version on PubMed Central for supplementary material.

ACKNOWLEDGMENTS

REFERENCES

Ayanga BA, Badal SS, Wang Y, Galvan DL, Chang BH, Schumacker PT, and Danesh FR (2016). Dynamin-related protein 1 deficiency improves mitochondrial fitness and protects against progression of diabetic nephropathy. J. Am. Soc. Nephrol 27, 2733–2747. [PubMed: 26825530]

Badal SS, Wang Y, Long J, Corcoran DL, Chang BH, Truong LD, Kanwar YS, Overbeek PA, and Danesh FR (2016). miR-93 regulates Msk2-mediated chromatin remodelling in diabetic nephropathy. Nat. Commun 7, 12076. [PubMed: 27350436]

Brinkkoetter PT, Bork T, Salou S, Liang W, Mizi A, Özel C, Koehler S, Hagmann HH, Ising C, Kuczkowski A, et al. (2019). Anaerobic glycolysis maintains the glomerular filtration barrier

independent of mitochondrial metabolism and dynamics. Cell Rep. 27, 1551–1566.e5. [PubMed: 31042480]

Caldwell RW, Rodriguez PC, Toque HA, Narayanan SP, and Caldwell RB (2018). Arginase: a multifaceted enzyme important in health and disease. Physiol. Rev 98, 641–665. [PubMed: 29412048]

Darshi M, Van Espen B, and Sharma K (2016). Metabolomics in Diabetic Kidney Disease: Unraveling the Biochemistry of a Silent Killer. Am. J. Nephrol 44, 92–103. [PubMed: 27410520]

Forbes JM, and Thorburn DR (2018). Mitochondrial dysfunction in diabetic kidney disease. Nat. Rev. Nephrol 14, 291–312. [PubMed: 29456246]

Fu A, Alvarez-Perez JC, Avizonis D, Kin T, Ficarro SB, Choi DW, Karakose E, Badur MG, Evans L, Rosselot C, et al. (2020). Glucose-dependent partitioning of arginine to the urea cycle protects β-cells from inflammation. Nat. Metab 2, 432–446. [PubMed: 32694660]

Galvan DL, Green NH, and Danesh FR (2017). The hallmarks of mitochondrial dysfunction in chronic kidney disease. Kidney Int. 92, 1051–1057. [PubMed: 28893420]

Galvan DL, Long J, Green N, Chang BH, Lin JS, Schumacker P, Truong LD, Overbeek P, and Danesh FR (2019). Drp1S600 phosphorylation regulates mitochondrial fission and progression of nephropathy in diabetic mice. J. Clin. Invest 129, 2807–2823. [PubMed: 31063459]

Geiger R, Rieckmann JC, Wolf T, Basso C, Feng Y, Fuhrer T, Kogadeeva M, Picotti P, Meissner F, Mann M, et al. (2016). L-Arginine modulates T cell metabolism and enhances survival and anti-tumor activity. Cell 167, 829–842.e13. [PubMed: 27745970]

Grody WW, Argyle C, Kern RM, Dizikes GJ, Spector EB, Strickland AD, Klein D, and Cederbaum SD (1989). Differential expression of the two human arginase genes in hyperargininemia. Enzymatic, pathologic, and molecular analysis. J. Clin. Invest 83, 602–609. [PubMed: 2913054]

Hallan S, and Sharma K (2016). The role of mitochondria in diabetic kidney disease. Curr. Diab. Rep 16, 61. [PubMed: 27155611]

Han SH, Wu MY, Nam BY, Park JT, Yoo TH, Kang SW, Park J, Chinga F, Li SY, and Susztak K (2017). PGC-1α protects from Notch-induced kidney fibrosis development. J. Am. Soc. Nephrol 28, 3312–3322. [PubMed: 28751525]

Hirayama A, Nakashima E, Sugimoto M, Akiyama S, Sato W, Maruyama S, Matsuo S, Tomita M, Yuzawa Y, and Soga T (2012). Metabolic profiling reveals new serum biomarkers for differentiating diabetic nephropathy. Anal. Bioanal. Chem 404, 3101–3109. [PubMed: 23052862]

Hong Q, Zhang L, Das B, Li Z, Liu B, Cai G, Chen X, Chuang PY, He JC, and Lee K (2018). Increased podocyte Sirtuin-1 function attenuates diabetic kidney injury. Kidney Int. 93, 1330–1343. [PubMed: 29477240]

Kato M, and Natarajan R (2019). Epigenetics and epigenomics in diabetic kidney disease and metabolic memory. Nat. Rev. Nephrol 15, 327–345. [PubMed: 30894700]

Kato M, Wang M, Chen Z, Bhatt K, Oh HJ, Lanting L, Deshpande S, Jia Y, Lai JY, O'Connor CL, et al. (2016). An endoplasmic reticulum stress-regulated lncRNA hosting a microRNA megacluster induces early features of diabetic nephropathy. Nat. Commun 7, 12864. [PubMed: 27686049]

Li SY, and Susztak K (2016). The long noncoding RNA Tug1 connects metabolic changes with kidney disease in podocytes. J. Clin. Invest 126, 4072–4075. [PubMed: 27760046]

Li S-Y, Park J, Qiu C, Han SH, Palmer MB, Arany Z, and Susztak K (2017). Increasing the level of peroxisome proliferator-activated receptor γ co-activator-1α in podocytes results in collapsing glomerulopathy. JCI Insight 2, e92930.

Lin J, Wu PH, Tarr PT, Lindenberg KS, St-Pierre J, Zhang CY, Mootha VK, Jäger S, Vianna CR, Reznick RM, et al. (2004). Defects in adaptive energy metabolism with CNS-linked hyperactivity in PGC-1alpha null mice. Cell 119, 121–135. [PubMed: 15454086]

Lin X, Duan X, Liang YY, Su Y, Wrighton KH, Long J, Hu M, Davis CM, Wang J, Brunicardi FC, et al. (2006). PPM1A functions as a Smad phosphatase to terminate TGFbeta signaling. Cell 125, 915–928. [PubMed: 16751101]

Livak KJ, and Schmittgen TD (2001). Analysis of relative gene expression data using real-time quantitative PCR and the 2(–Delta Delta C(T)) Method. Methods 25, 402–408. [PubMed: 11846609]

Long J, and Danesh FR (2018). Values and limitations of targeting lncRNAs in diabetic nephropathy. Diabetes 67, 552–553. [PubMed: 29559513]

Long J, Badal SS, Ye Z, Wang Y, Ayanga BA, Galvan DL, Green NH, Chang BH, Overbeek PA, and Danesh FR (2016). Long noncoding RNA Tug1 regulates mitochondrial bioenergetics in diabetic nephropathy. J. Clin. Invest 126, 4205–4218. [PubMed: 27760051]

Long J, Galvan DL, Mise K, Kanwar YS, Li L, Poungavrin N, Overbeek PA, Chang BH, and Danesh FR (2020). Role for carbohydrate response element-binding protein (ChREBP) in high glucose-mediated repression of long noncoding RNA Tug1. J. Biol. Chem 295, 15840–15852. [PubMed: 32467232]

Martin OJ, Lai L, Soundarapandian MM, Leone TC, Zorzano A, Keller MP, Attie AD, Muoio DM, and Kelly DP (2014). A role for peroxisome proliferator-activated receptor γ coactivator-1 in the control of mitochondrial dynamics during postnatal cardiac growth. Circ. Res 114, 626–636. [PubMed: 24366168]

Martínez-Reyes I, and Chandel NS (2020). Mitochondrial TCA cycle metabolites control physiology and disease. Nat. Commun 11, 102. [PubMed: 31900386]

Morris SM Jr., Bhamidipati D, and Kepka-Lenhart D (1997). Human type II arginase: sequence analysis and tissue-specific expression. Gene 193, 157–161. [PubMed: 9256072]

Morris SM Jr., Gao T, Cooper TK, Kepka-Lenhart D, and Awad AS (2011). Arginase-2 mediates diabetic renal injury. Diabetes 60, 3015–3022. [PubMed: 21926276]

Mundel P, Reiser J, Zúñiga Mejía Borja A, Pavenstädt H, Davidson GR, Kriz W, and Zeller R (1997). Rearrangements of the cytoskeleton and cell contacts induce process formation during differentiation of conditionally immortalized mouse podocyte cell lines. Exp. Cell Res 236, 248–258. [PubMed: 9344605]

Ochocki JD, Khare S, Hess M, Ackerman D, Qiu B, Daisak JI, Worth AJ, Lin N, Lee P, Xie H, et al. (2018). Arginase 2 suppresses renal carcinoma progression via biosynthetic cofactor pyridoxal phosphate depletion and increased polyamine toxicity. Cell Metab. 27, 1263–1280.e6. [PubMed: 29754953]

Qi W, Keenan HA, Li Q, Ishikado A, Kannt A, Sadowski T, Yorek MA, Wu IH, Lockhart S, Coppey LJ, et al. (2017). Pyruvate kinase M2 activation may protect against the progression of diabetic glomerular pathology and mitochondrial dysfunction. Nat. Med 23, 753–762. [PubMed: 28436957]

Ransohoff JD, Wei Y, and Khavari PA (2018). The functions and unique features of long intergenic non-coding RNA. Nat. Rev. Mol. Cell Biol 19, 143–157. [PubMed: 29138516]

Singh SP, Schragenheim J, Cao J, Falck JR, Abraham NG, and Bell-ner L (2016). PGC-1 alpha regulates HO-1 expression, mitochondrial dynamics and biogenesis: Role of epoxyeicosatrienoic acid. Prostaglandins Other Lipid Mediat. 125, 8–18. [PubMed: 27418542]

Statello L, Guo C-J, Chen L-L, and Huarte M (2021). Gene regulation by long non-coding RNAs and its biological functions. Nat. Rev. Mol. Cell Biol 22, 96–118. [PubMed: 33353982]

Sun SF, Tang PMK, Feng M, Xiao J, Huang XR, Li P, Ma RCW, and Lan HY (2018). Novel lncRNA Erbb4-IR Promotes Diabetic Kidney Injury in *db/db* Mice by Targeting miR-29b. Diabetes 67, 731–744. [PubMed: 29222368]

Tran MT, Zsengeller ZK, Berg AH, Khankin EV, Bhasin MK, Kim W, Clish CB, Stillman IE, Karumanchi SA, Rhee EP, and Parikh SM (2016). PGC1α drives NAD biosynthesis linking oxidative metabolism to renal protection. Nature 531, 528–532. [PubMed: 26982719]

Ulitsky I, and Bartel DP (2013). lincRNAs: genomics, evolution, and mechanisms. Cell 154, 26–46. [PubMed: 23827673]

Vockley JG, Jenkinson CP, Shukla H, Kern RM, Grody WW, and Cederbaum SD (1996). Cloning and characterization of the human type II arginase gene. Genomics 38, 118–123. [PubMed: 8954792]

Wang J, Wang Y, Long J, Chang BH, Wilson MH, Overbeek P, and Danesh FR (2010). Tamoxifen-inducible podocyte-specific iCre recombinase transgenic mouse provides a simple approach for modulation of podocytes *in vivo*. Genesis 48, 446–451. [PubMed: 20641128]

Wang W, Wang Y, Long J, Wang J, Haudek SB, Overbeek P, Chang BH, Schumacker PT, and Danesh FR (2012). Mitochondrial fission triggered by hyperglycemia is mediated by ROCK1 activation in podocytes and endothelial cells. Cell Metab. 15, 186–200. [PubMed: 22326220]

Wetzel MD, Stanley K, Wang WW, Maity S, Madesh M, Reeves WB, and Awad AS (2020). Selective inhibition of arginase-2 in endothelial cells but not proximal tubules reduces renal fibrosis. JCI Insight 5, e142187.

Xu W, Ghosh S, Comhair SA, Asosingh K, Janocha AJ, Mavrakis DA, Bennett CD, Gruca LL, Graham BB, Queisser KA, et al. (2016). Increased mitochondrial arginine metabolism supports bioenergetics in asthma. J. Clin. Invest 126, 2465–2481. [PubMed: 27214549]

You H, Gao T, Cooper TK, Morris SM Jr., and Awad AS (2013). Arginase inhibition mediates renal tissue protection in diabetic nephropathy by a nitric oxide synthase 3-dependent mechanism. Kidney Int. 84, 1189–1197. [PubMed: 23760286]

Zhang T, Chi Y, Kang Y, Lu H, Niu H, Liu W, and Li Y (2019). Resveratrol ameliorates podocyte damage in diabetic mice via SIRT1/PGC-1α mediated attenuation of mitochondrial oxidative stress. J. Cell. Physiol 234, 5033–5043. [PubMed: 30187480]

Zhou D, Zhou M, Wang Z, Fu Y, Jia M, Wang X, Liu M, Zhang Y, Sun Y, Lu Y, et al. (2019). PGRN acts as a novel regulator of mitochondrial homeostasis by facilitating mitophagy and mitochondrial biogenesis to prevent podocyte injury in diabetic nephropathy. Cell Death Dis. 10, 524. [PubMed: 31285425]

Highlights

- Tug1/PGC1α improves mitochondrial bioenergetics, biogenesis, and dynamics in podocytes

- PGC1α deficiency mitigates the renoprotective effects of lncRNA Tug1 in diabetic mice

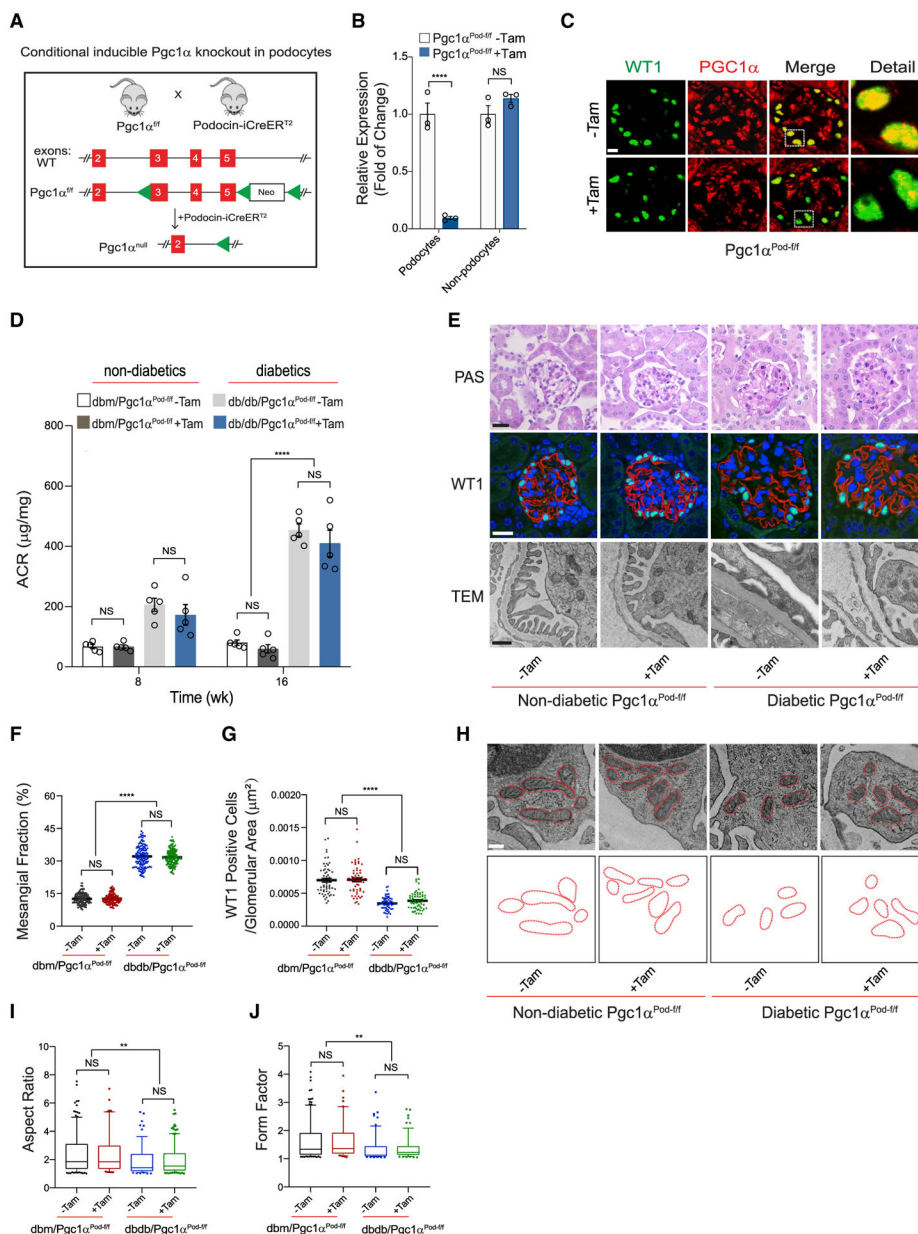- Urea cycle metabolites and arginase 2 link Tug1/PGC1α axis to mitochondrial remodeling

Figure 1. Conditional and inducible deletion of *Pgc1α* in podocytes does not exacerbate progression of DN

(A) Schematic of the podocyte-specific tamoxifen-inducible Pgc1α knockout strategy using the Cre-LoxP system.

(B) qRT-PCR analysis of *Pgc1α* gene expression in isolated primary podocyte or nonpodocyte fractions from podocyte-specific control (−Tam) and tamoxifen-treated (+Tam) Pgc1α knockout mice (n = 3 mice/group).

(C) Representative immunofluorescence micrographs of kidney sections stained with WT1 (green) and PGC1α (red) antibodies. Scale, 25 μm.

(D) ACR analysis of tamoxifen-induced and noninduced controls from nondiabetic (db/m; Pgc1α$^{Pod-f/f}$) and diabetic (db/db; Pgc1α$^{Pod-f/f}$) mice at 8 and 16 weeks of age (n = 5 mice/ group).

(E) Representative images of PAS staining (upper panel), WT1 staining (middle panel), and TEM (bottom panel) of kidney glomeruli from groups described in (D). Scales, 50 μm (upper and middle panels) and 0.5 μm (bottom panel).

(F and G) Quantification of mesangial matrix expansion (F) and WT1-positive cells/ glomerular area (G) in the respective group. n = 3 independent animals per group.

(H) Representative TEM micrographs (upper panel) and tracing (lower panel) of the mitochondria in podocytes from the indicated experimental groups. Scale, 0.2 μm.

(I and J) Average mitochondrial aspect ratios (I) and form factors (J) from TEM micrographs of groups described in (H, upper panel). n = 3 independent mice per group.

Results are presented as mean ± SEMs (B, D, F, and G). Boxes represent median with interquartile range (IQR), and whiskers represent a 5–95 percentile range (I and J). Data were analyzed for statistical significance using one-way ANOVA followed by Tukey's multiple comparison test (D, F, G, I, and J) or using two-tailed t test (B). $**p < 0.01$; $****p < 0.0001$; NS, not significant.
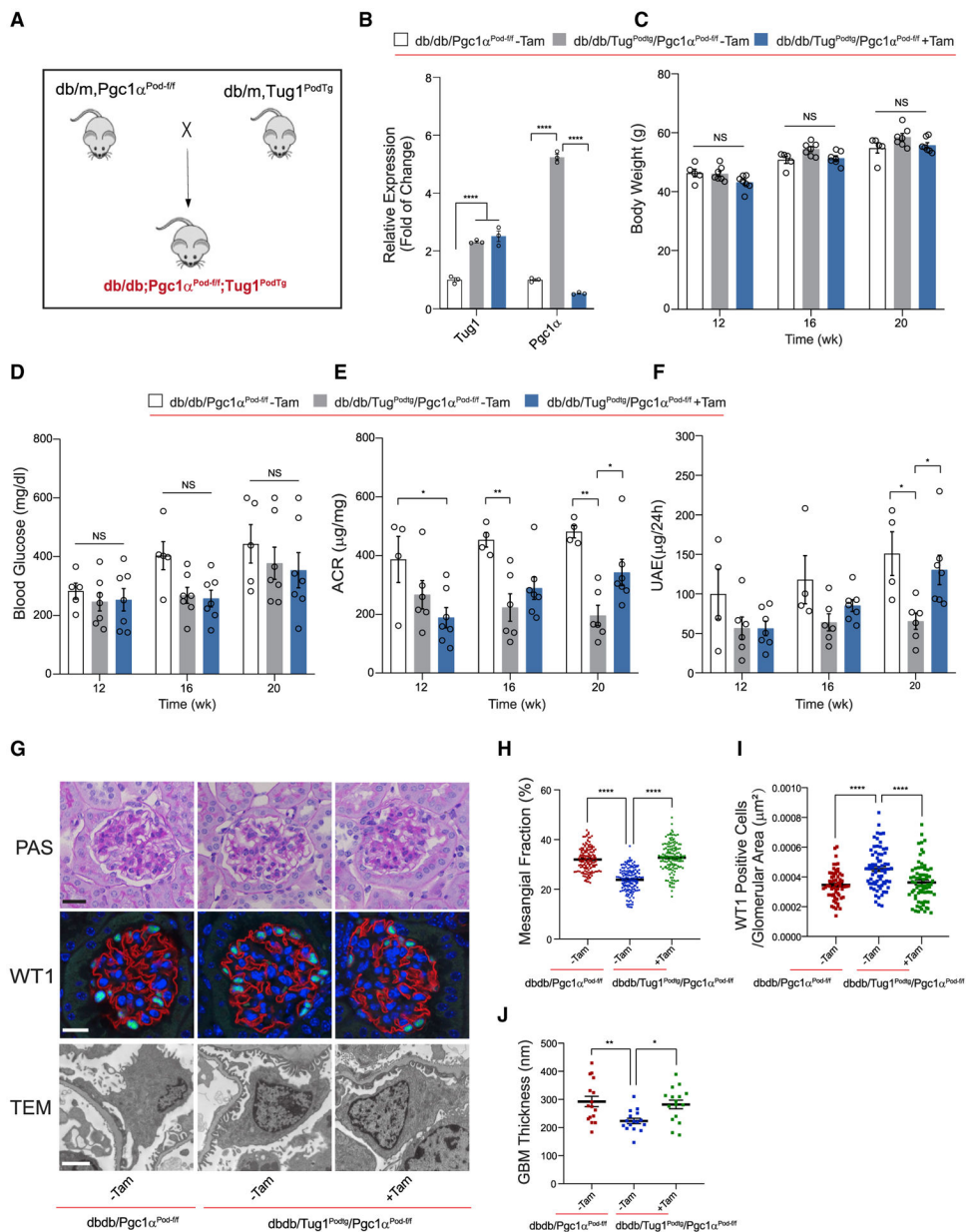
Figure 2. Podocyte-specific *Pgc1α* deficiency mitigates the renoprotective effect of podocyte-specific lncRNA *Tug1* transgenic mice in the diabetic *db/db* model

(A) Schematic of the mating strategy for diabetic *db/db* mice with podocyte-specific lncRNA *Tug1* transgenic and *Pgc1α* knockout.

(B) qRT-PCR analysis of *Tug1* and *Pgc1α* gene expression in the primary podocytes isolated from the indicated mice (n = 3 mice per group).

(C–F) Body weight (C), blood glucose (D), ACR (E), and 24 h urine albumin excretion (UAE) (F) analysis of diabetic podocyte-specific Pgc1α-floxed control (db/db; Pgc1α$^{Pod-f/f}$, n = 4 or 5 mice/group) and –Tam (n = 6 or 7 mice/group) or +Tam (n = 7 mice/group) diabetic podocyte-specific Pgc1α-floxed plus Tug1 transgenic (db/db; Tug1^{Pod-tg}; Pgc1α$^{Pod-f/f}$) mice at 12, 16, and 20 weeks of age.

(G) Representative images of PAS staining (upper panel), WT1 staining (middle panel), and TEM (bottom panel) of kidney glomeruli from different experimental groups. Scales, 50 μm (upper and middle panels) and 2 μm (bottom panel).

(H–J) Quantification of mesangial matrix expansion (H), WT1-positive cells/glomerular area (I), and GBM thickness (J) from images represented in (G). n = 3 independent mice per group; n = 50 glomeruli analyzed per mouse in (H), n = 20 glomeruli analyzed per mouse in (I), and n = 5 micrographs analyzed per mouse in (J). Results are presented as mean ± SEMs. $*p < 0.05$; $**p < 0.01$; $****p < 0.0001$; NS, not significant, by one-way ANOVA followed by Tukey's multiple comparison test.
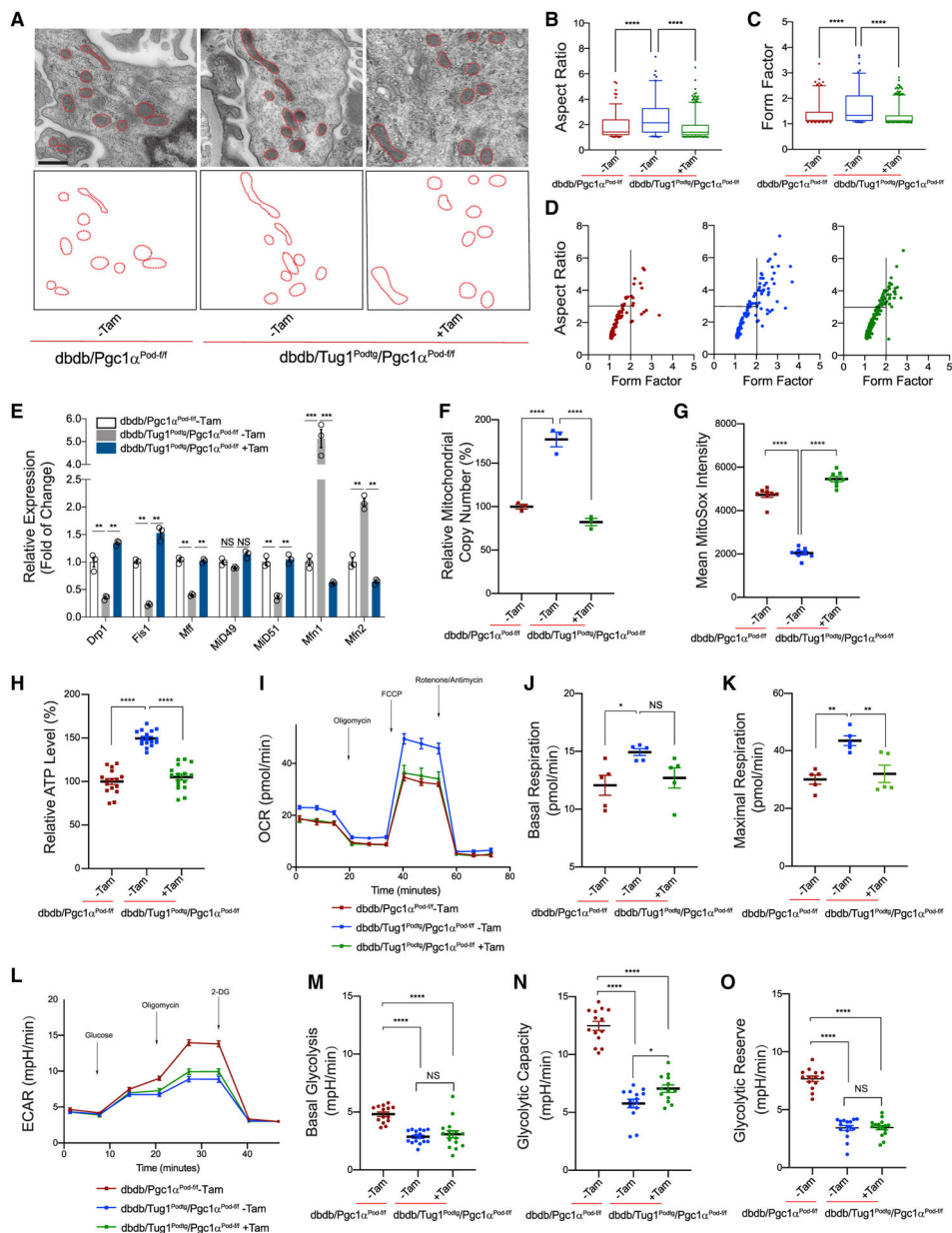
Figure 3. lncRNA *Tug1*-mediated mitochondrial fitness in podocytes is reversed with *Pgc1α* knockout

(A) Representative TEM micrograph (upper panel) and tracing (lower panel) of mitochondria in podocytes of the experimental mice with the indicated genotypes. Scale, 0.5 μm.

(B–D) Quantification of podocyte mitochondrial aspect ratio (B), form factor (C), and aspect ratio plotted against form factor (D) from TEM images of different experimental groups. n = 4 independent mice per group.

(E) qRT-PCR analysis of mitochondrial dynamics-related genes in isolated primary podocytes.

(F–H) Mitochondrial function as assessed by mitochondrial copy number (F), MitoSOX production (G), and total ATP production (H) in isolated primary podocytes. (I–K) Seahorse

analysis of OCR (I), with basal respiration (J) and maximal respiration (K) from isolated primary podocytes.

(L–O) Seahorse analysis of ECAR (L), with basal glycolysis (M), glycolytic capacity (N), and glycolytic reserve (O) from isolated primary podocytes.

Boxes represent median with IQR, and whiskers represent a 5–95 percentile range (B and C). Lines and error bars represent mean $\pm$ SEMs (E–O). Data were analyzed by one-way ANOVA with Tukey's multiple comparison test. $*p < 0.05$; $**p < 0.01$; $***p < 0.001$; $****p < 0.0001$; NS, not significant.
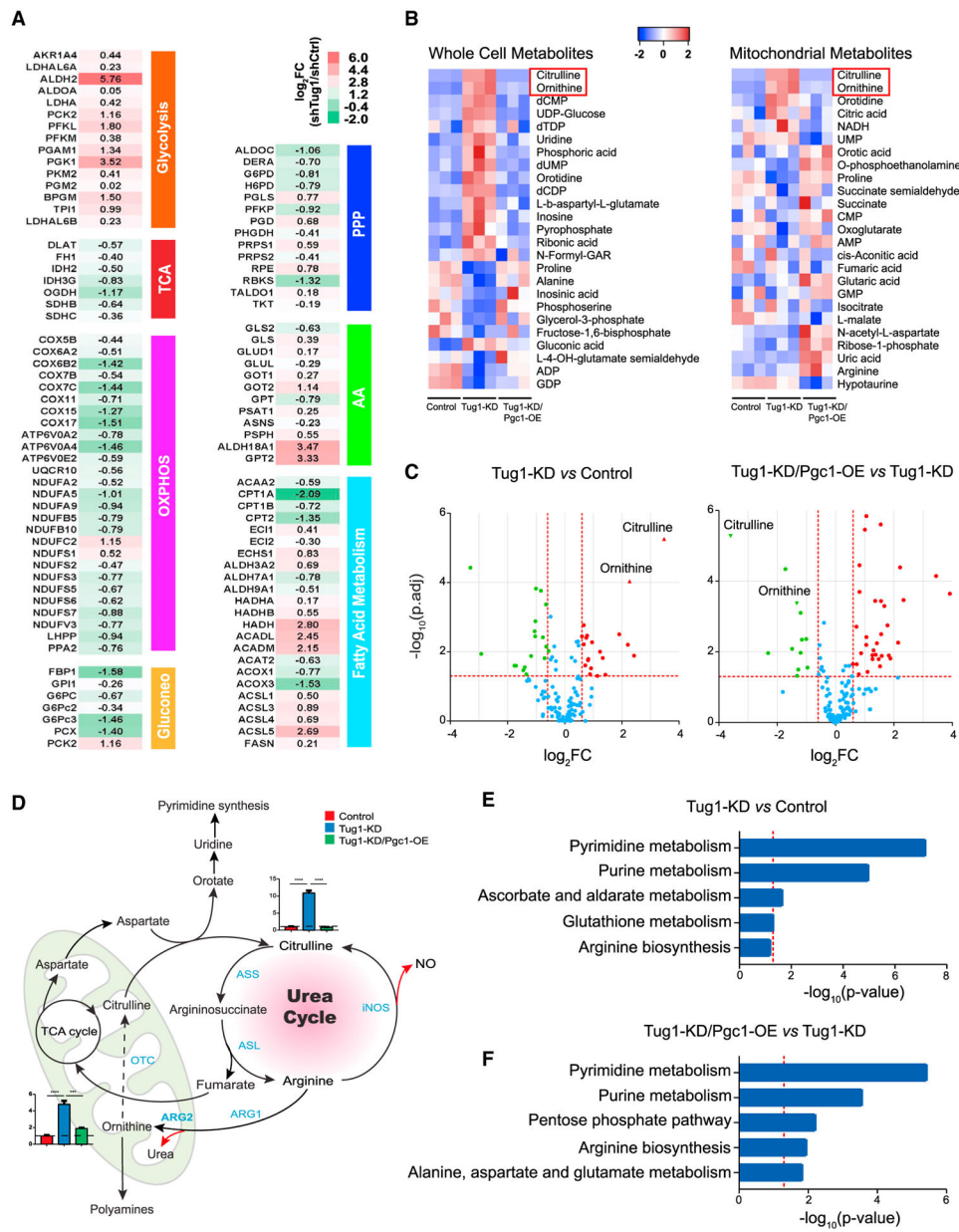
Figure 4. Urea cycle intermediates link the Tug1/PGC1α axis with mitochondrial remodeling

(A) Microarray analysis of key metabolic enzymes of multiple metabolic pathways between stable Tug1-knockdown versus shRNA control (shTug1 versus shCtrl) podocytes.

(B) Heatmap of the top 25 whole-cell mitochondrial metabolites that differ among control, Tug1-KD, and Tug1-KD with Pgc1α-OE podocytes.

(C) Volcano plots of metabolomic data generated from Tug1-KD podocytes compared with control, as well as Tug1-KD/Pgc1-OE podocytes compared with Tug1-KD cells. Significantly (adjusted $p < 0.05$) regulated metabolites with a cutoff of a log_2 fold change greater than 1.5 are marked in green (downregulated) and red (upregulated).

(D) Schematic of the urea cycle and links among arginine metabolism, the TCA cycle, and the pyrimidine synthesis pathway. Relative levels of ornithine and citrulline are shown.

Samples are normalized to control cells, as indicated by dashed lines in the bar graphs. Valued are presented as mean ± SEMs. ***$p < 0.001$; ****$p < 0.0001$, by one-way ANOVA followed by Tukey's multiple comparison test. ARG1, arginase 1; ARG2, arginase 2; ASS, argininosuccinate synthetase; ASL, argininosuccinate lyase; iNOS (NOS2), inducible nitric oxide synthase; OTC, ornithine transcarbamylase.

(E and F) Metabolite set enrichment analysis of the significantly regulated metabolic pathways in Tug1-KD podocytes compared with controls and in Tug1-KD/Pgc1-OE podocytes compared with Tug1-KD cells. The dashed line indicates $p < 0.05$.
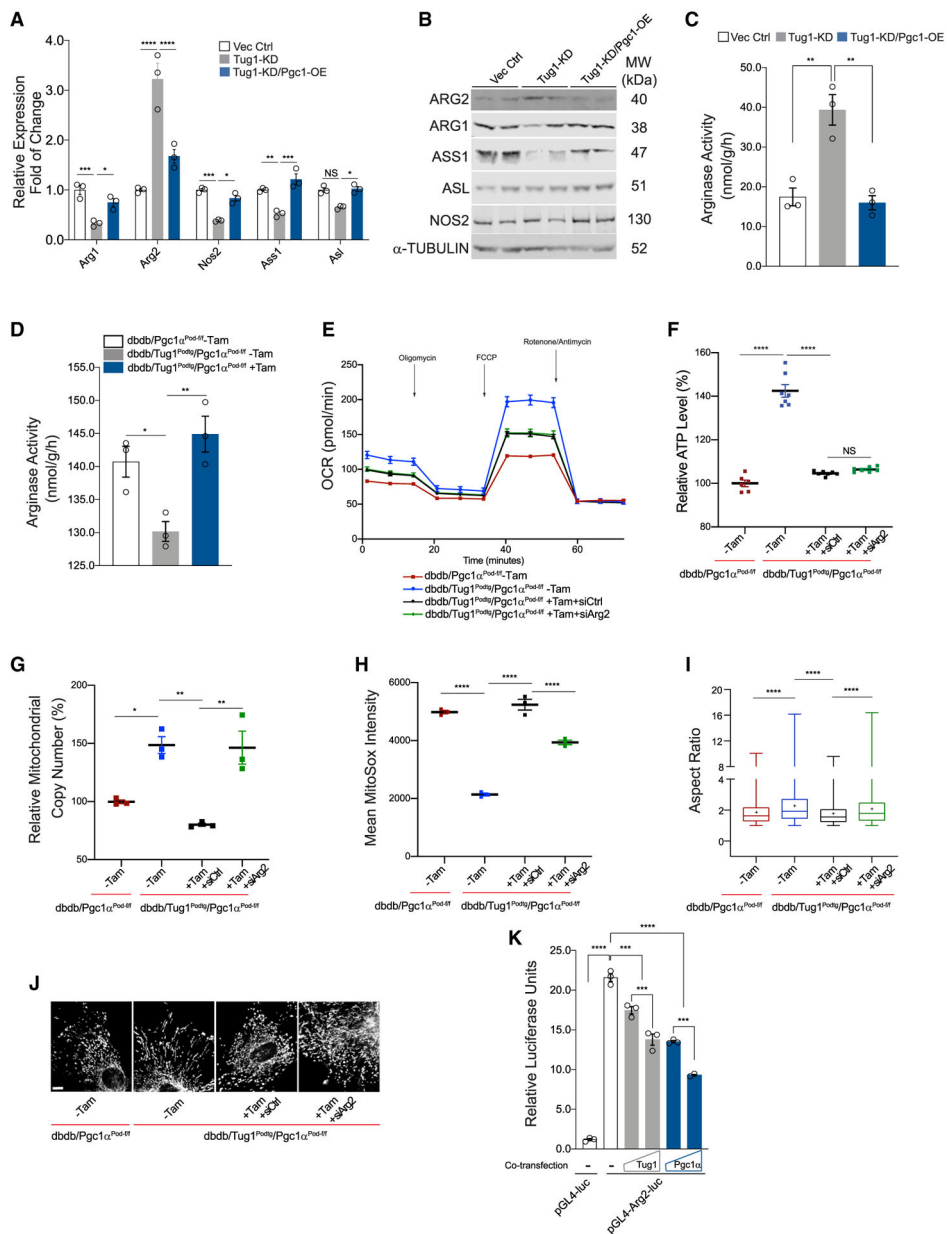
Figure 5. Mitochondrial arginase 2 links the Tug1/PGC1α axis with mitochondrial metabolism
(A) qRT-PCR analysis of key enzymes in the urea cycle in control, Tug1-KD, and Tug1-KD/
Pgc1-OE podocytes.

(B) Western blot analysis of key enzymes in the urea cycle from the indicated podocyte cell
lines.

(C) Arginase activity assay from the indicated podocyte cell lines.

(D) Arginase activity assay from the indicated primary podocytes.

(E–J) Mitochondrial function as assessed by Seahorse analysis of OCR (E), total ATP
production (F), mitochondrial copy number (G), MitoSOX production (H), mitochondrial
aspect ratio (I), and representative images of mitochondria morphology with MitoTracker
staining (J) in isolated primary podocytes from db/db; Pgc1α$^{Pod-f/f}$ –Tam mice, db/db;

Tug1^{Pod-tg}; Pgc1$\alpha^{Pod-f/f}$ –Tam mice, and db/db; Tug1^{Pod-tg}; Pgc1$\alpha^{Pod-f/f}$ +Tam mice with control siRNA (+siCtrl) or Arg2 siRNA (+siArg2) transfection. Scale in (J), 10 μm.

(K) Arg2 promoter luciferase reporter assay in HEK293T cells cotransfected with an increasing amount of Tug1 or Pgc1α for transient overexpression. Results are presented as mean ± SEMs. (I) Box, median with IQR; whiskers, min to max; +, mean value. $*p < 0.05$; $**p < 0.01$; $***p < 0.001$; $****p < 0.0001$; NS, not significant, by one-way ANOVA followed by Tukey's multiple comparison test.

KEY RESOURCES TABLE

REAGENT or RESOURCE	SOURCE	IDENTIFIER
Antibodies		
Donkey anti–mouse Alexa Fluor 488	Thermo Fisher	Cat# A21202; RRID: AB_141607
Donkey anti–mouse Alexa Fluor 594	Thermo Fisher	Cat# A21203; RRID: AB_141633
Donkey anti–rabbit Alexa Fluor 488	Thermo Fisher	Cat# A21206; RRID: AB_2535792
Donkey anti–rabbit Alexa Fluor 594	Thermo Fisher	Cat# A21207; RRID: AB_141637
Donkey anti–rabbit Alexa Fluor 647	Thermo Fisher	Cat# A21244; RRID: AB_141663
Goat anti-guinea pig Alexa Fluor 594	Thermo Fisher	Cat# A11076; RRID: AB_2534120
Goat anti–mouse DyLight 680	Thermo Fisher	Cat# 35519; RRID: AB_1965956
Goat anti–mouse DyLight 800	Thermo Fisher	Cat# SA510172; RRID: AB_2556752
Goat anti-Podocalyxin, biotinylated	R&D Systems	Cat# BAF1556; RRID: AB_356043
Goat anti–rabbit DyLight 680	Thermo Fisher	Cat# 35519; RRID: AB_1965956
Goat anti–rabbit DyLight 800	Thermo Fisher	Cat# SA535571; RRID: AB_2556775
Guinea pig anti-Synaptopodin (SYNPO)	Progen	Cat# GP94-N; RRID: AB_2811107
Mouse anti-β-ACTIN	Cell Signaling	Cat# 4967; RRID: AB_330288
Mouse anti-ARG1	Santa Cruz	Cat# 271430; RRID: AB_10648473
Mouse anti-ARG2	Santa Cruz	Cat# sc- 393496; RRID: AB_2890065
Mouse anti-ASL	Santa Cruz	Cat# sc-166787; RRID: AB_2274349
Mouse anti-ASS1	Santa Cruz	Cat# sc-365475; RRID: AB_10847087
Mouse anti–FLAG M2 monoclonal	Sigma-Aldrich	Cat# F3165; RRID: AB_259529
Mouse anti-NOS2	Santa Cruz	Cat# sc-7271; RRID: AB_627810
Mouse anti-PGC1α	Millipore Sigma	Cat# ST1202; RRID: AB_2237237
Rabbit anti-PGC1α	Novus Biologicals	Cat# NBP1-04676; RRID: AB_1522118
Mouse anti-PGC1β	Santa Cruz	Cat# sc-373771; RRID: AB_10915290
Rabbit anti-NOS3 (eNOS)	Thermo Fisher	Cat# PA3-031A; RRID: AB_225144
Rabbit anti-α-TUBULIN	Cell Signaling	Cat# 2144; RRID: AB_2210548
Rabbit anti-Wilms Tumor Protein (WT1)	Abcam	Cat# ab89901; RRID: AB_1965956
Sheep anti-KIRREL3, biotinylated	R&D Systems	Cat# BAF4910; RRID: AB_2044689
Chemicals, peptides, and recombinant proteins		
Collagen I, rat tail	Thermo Fisher	Cat# A10483-01
Collagenase, type I	Worthington	Cat# CLS-1
Collagenase/Dispase	Roche	Cat# 11097113001
DAPI	Thermo Fisher	Cat# 62248
D-(+)-Glucose Solution, 40%	TEKnova	Cat# G2020
DNase I (RNase-free)	New England Biolabs	Cat# M0303L
GoTaq Green Master Mix	Promega	Cat# M7123
L-Arginine	Sigma-Aldrich	Cat# A8094
L-Citrulline	Sigma-Aldrich	Cat# C7629

REAGENT or RESOURCE	SOURCE	IDENTIFIER
L-Ornithine monohydrochloride	Sigma-Aldrich	Cat# O6503
Lipofectamine 2000	Thermo Fisher	Cat# 11668027
MitoSOX Red	Thermo Fisher	Cat# M36008
Mouse recombinant IFN-γ	Millipore Sigma	Cat# I4777
PowerUp SYBR Green Master Mix	Thermo Fisher	Cat# A25742
Puromycin	Sigma-Aldrich	Cat# P8833
S-(2-boronoethyl)-L-cysteine (BEC)	Cayman Chemical	Cat# 22145
Tamoxifen	Sigma-Aldrich	Cat# T5648
TaqPath ProAmp Master Mix	Thermo Fisher	Cat# A30866
Critical commercial assays		
CellTiter-Glo Luminescent Cell Viability Assay Kit	Promega	Cat# G7570
Custom TaqMan Copy Number Assay, mouse, Tug1-Podtg	Thermo Fisher	Cat# 4400295 Assay ID# Pod-Tug1_CD47V4J
Custom TaqMan SNP Genotyping Assay, mouse, Lepr	Thermo Fisher	Cat# 4332075 Assay ID# AH5I6UF
DC Protein Assay Kit II	Bio-Rad	Cat# 5000112
Dual Luciferase (Firefly-Renilla) Assay System	BPS Bioscience	Cat# 60683-1
iScript cDNA Synthesis Kit	Bio-Rad	Cat# 1708891
Mouse albumin ELISA Kit	Exocell	Cat# 1011
PureLink Genomic DNA Mini Kit	Thermo Fisher	Cat# K182000
PureLink RNA Mini Kit	Thermo Fisher	Cat# 12183020
QuantiChrom Arginase Assay Kit	BioAssay Systems	Cat# DARG-100
QuantiChrom Creatinine Assay Kit	BioAssay Systems	Cat# DICT500
Steady-Glo Luciferase Assay System	Promega	Cat# E2510
Seahorse XFe96 FluxPak	Agilent	Cat# 02416-100
Seahorse XF Cell Mito Stress Test Kit	Agilent	Cat# 103015-100
Seahorse XF Glycolysis Stress Test Kit	Agilent	Cat# 103020-100
TaqMan Copy Number Reference Assay, mouse, Tfrc	Thermo Fisher	Cat# 4458367
TaqMan Copy Number Reference Assay, mouse, Tert	Thermo Fisher	Cat# 4458369
Deposited data		
Metabolomics Workbench data repository; PR001167	NIH	
Experimental models: Cell lines		
Mouse Podocyte Clone-5 (MPC5)	Mundel et al., 1997	RRID: CVCL_AS87
MPC-Vector Control	Long et al., 2016	N/A
MPC-Tug1-KD	Long et al., 2016	N/A
MPC-Tug1-KD/Pgc1-OE	This paper	N/A
HEK293T	ATCC	Cat# CRL-3216; RRID: CVCL_0063
Experimental models: Organisms/strains		
Mouse: C57BL/6J	Jackson Laboratory	IMSR Cat# JAX_000664; RRID: IMSR_JAX:000664
Mouse: db/db (BKS.Cg-$Dock7^m$+/+$Lepr^{db}$/J)	Jackson Laboratory	IMSR Cat# JAX_000642; RRID: IMSR_JAX:000642
Mouse: Podocin-iCreER^{T2}	Wang et al., 2010	RRID: MGI_4819592

REAGENT or RESOURCE	SOURCE	IDENTIFIER
Mouse: *Ppargc1a*^fl/fl (B6N.129(FVB)-Ppargc1a^tm2.1Brsp/J)	Jackson Laboratory	IMSR Cat# JAX_009666; RRID: IMSR_JAX:009666
Mouse: Tug1^Podtg	Long et al., 2016	N/A
Oligonucleotides		
Primers for qRT-PCR, see Table S1	This paper	N/A
Primer for genotyping: murine iCre-Podtg, forward primer: 5'-TCAACATGCTGCAC AGGAGA-3'	This paper	N/A
Primer for genotyping: murine iCre-Podtg, forward primer: 5'-CCTTCACTCTGATT CTGGCA-3'	This paper	N/A
Primer for genotyping: murine Ppargc1a, forward primer: 5'-ATTTGTGAGTGCGC AGTGATGA–3'	This paper	N/A
Primer for genotyping: murine Ppargc1a, reverse primer: 5'-TGCCTTCTGTTTCTA ACTCAGG-3'	This paper	N/A
Primer for genotyping: murine Tug1- Podtg, forward primer: 5'-CACCCG ACG GTCTTTAGGGT-3'	Long et al., 2016	N/A
Primer for genotyping: murine Tug1-Podtg, reverse primer: 5'-CCTTCTCCAG AGGAAAGCCT-3'	Long et al., 2016	N/A
Primer for PCR cloning: murine Arg2 1kb proximal promoter, forward primer: 5'-TC GGTACCTCTAGTAACCAGTGCTCTT-3'	This paper	N/A
Primer for PCR cloning: murine Arg2 1kb proximal promoter, reverse primer: 5'-TC GTCGACCTGTCCCCGAGAGAAAGG-3'	This paper	N/A
siRNA targeting sequence: murine Arg2, 5'-UAUAGCUACAGAGUGGACGga-3'	Ambion (Thermo Fisher)	Cat# 4390771 siRNA ID# s62582
Recombinant DNA		
pcDNA-f:PGC1	Addgene	Cat# 1026
pGL4.10[luc2]	Promega	Cat# E6651
pGL4-Arg2-luc	This paper	N/A
pRK5	Lin et al., 2006	N/A
pRK5-Pgc1α	This paper	N/A
pRK5-Tug1	Long et al., 2016	N/A
Zeo-pT-MCS-GFP-T2A-Puro	Long et al., 2020	N/A
Zeo-pT-Flag-Pgc1a-Puro	This paper	N/A
Software and algorithms		
Adobe Photoshop CC 2020	Adobe Systems	RRID: SCR_014199
ImageJ v1.51	NIH	RRID: SCR_003070
Image Studio Lite	Li-COR Biosciences	RRID: SCR_013715
Prism v8.0	GraphPad Software	RRID: SCR_002798
Seahorse Wave v2.6.1	Agilent	RRID: SCR_014526
Other		
DMEM	Corning	Cat# 10-014-CV
Dynabeads M-280 Streptavidin	Thermo Fisher	Cat# 11205D
FBS Opti-gold	GenDepot	Cat# F0900-050S
Nitrocellulose/Filter Paper Sandwiches	Bio-Rad	Cat# 1620215
ProLong Gold Antifade Mounting Reagent	Molecular Probes	Cat# P36934
RIPA buffer	TEKnova	Cat# R3792